Cellulose
https://doi.org/10.1007/s10570-025-06477-z

ORIGINAL RESEARCH

Key insights into TEMPO-mediated oxidation of cellulose: influence of starting material

André Mazega · Anna F. Lehrhofer · Roberto J. Aguado · Antje Potthast · Ronald Marquez · Thomas Rosenau · Marc Delgado-Aguilar

Received: 27 January 2025 / Accepted: 2 March 2025

Abstract The present study investigates the intricate relationships between the properties of cellulose nanomaterials (CNMs) and the lignocellulosic feedstocks from which they are derived. The starting pulps, consisting of eucalyptus, pine, hemp, and sisal commercial bleached pulps where characterized, and later subjected to TEMPO-mediated oxidation at several concentrations, followed by mechanical treatment in a high-pressure homogenizer. The resulting CNMs were extensively analyzed to assess carboxyl content, nanofibrillation yield, optical transmittance, and rheological and structural properties through methods including X-ray diffraction, X-ray photoelectron spectroscopy, solid-state ^{13}C nuclear magnetic resonance, and sugar composition analysis post-acidic methanolysis. Despite the consistent processing conditions, the study reveals significant differences in the physicochemical and rheological behaviors of CNMs, strongly linked to the inherent properties of their respective feedstocks. These disparities highlight the pivotal influence of feedstock characteristics on the final attributes of CNMs, while most of the previous works linked these differences either to chemical or structural differences. The findings suggest that optimizing CNM properties for specific applications requires precise control over feedstock selection and processing parameters, underscoring the critical role of material origin in the development and application of advanced nanomaterials.

Keywords Cellulose nanofibers · TEMPO-mediated oxidation · Lignocellulosic feedstocks · Rheology · Structural characterization

Supplementary Information The online version contains supplementary material available at https://doi.org/10.1007/s10570-025-06477-z.

A. Mazega · R. J. Aguado · R. Marquez · M. Delgado-Aguilar (✉)
LEPAMAP-PRODIS Research Group, University of Girona, C/Maria Aurèlia Capmany, 61, 17003 Girona, Spain
e-mail: m.delgado@udg.edu

A. F. Lehrhofer · A. Potthast · T. Rosenau
Institute of Chemistry of Renewable Resources, Department of Chemistry, University of Natural Resources and Life Sciences (BOKU), Muthgasse, 18, 1190 Vienna, Austria

Introduction

Understanding the fundamental structure of lignocellulosic fibers is crucial when selecting the feedstock for cellulose nanomaterial (CNM) production, as the chemical composition, accessibility, and structural properties directly influence processing efficiency and the quality of the resulting CNMs (Signori-Iamin et al. 2023; Hu et al. 2024). The use of raw materials alternative to wood, such as agricultural residues or annual plants, for CNM production has been a topic of great interest during the last decade (Aguado et al. 2022; Pradhan et al. 2022). Feedstock availability,

Published online: 20 March 2025

regional resource management, and logistics play a critical role in market dynamics, influencing production scalability and economic feasibility. Balancing these factors is essential to develop a sustainable and competitive CNM market capable of meeting increasing industrial demand across various sectors (Balea et al. 2020).

The impact of the choice of feedstock on both the production process and the resulting CNM properties has been only cursorily addressed in the literature (Aguado et al. 2022; Alila et al. 2013; Bettaieb et al. 2015). Most studies exploring raw material alternatives to wood for CNF production tend to emphasize the advantages of the feedstock's origin, while paying less attention to the potential benefits that its structural properties and chemical composition could offer. Both wood and non-wood plants contain the same macroconstituents (*e.g.*, lignin, hemicellulose, cellulose), but their content, the hemicelluloses' monosaccharide composition, lignin monomer composition and linkage structure and other structural characteristics are different, such as microfibril angle, lumen diameter, cell wall thickness, and crystallinity (Ludueña et al. 2013). Annual plants, such as jute, sisal, or hemp, usually exhibit lower lignin contents, shorter growing cycles with moderate irrigation requirements, and are thus usually intended for higher value-added applications than wood fibers (Manian et al. 2021; Serra-Parareda et al. 2021).

The structure of plant cell walls significantly influences fiber properties and their suitability for specific processes. Wood pulp fibers, with rigid and lignified cell walls, are particularly durable, while fibers from annual plants tend to be strong yet flexible. More specifically, eucalyptus wood fibers, being short with thin cell walls, are less resistant to chemical breakdown, making them easier to delignify and bleach (Morais et al. 2021). Pine fibers, which are longer and stronger, exhibit higher recalcitrance in pulping and bleaching due to their thicker cell walls and greater lignin content, requiring more intensive treatments (Singh et al. 2013). Hemp fibers are long, strong, and high in cellulose content, with lower recalcitrance, making them suitable for bio-composites and textiles (Manian et al. 2021). Sisal fibers, though also long and strong, are more rigid and recalcitrant, making them more challenging to bleach and ideal for sturdy industrial uses, such as ropes and mats (Aracri et al. 2011). Although determining the suitability for different industrial processes (Salmén, 2022), these features, broadly known and adequately understood for selecting the most appropriate application, have not been translated into the nanofiber domain.

One of the most well-known and broadly implemented process for CNF production is TEMPO-mediated oxidation. This largely regioselective oxidation consists of oxidizing the primary alcohol located at the gluyopyranoses' C-6 to an aldehyde, to be later converted into a carboxyl group (Saito and Isogai 2004). This oxidative treatment is usually performed on bleached fibers, ensuring the oxidation targets cellulose, specifically, while enhancing porosity and accessibility for subsequent uniform functionalization. However, the presence of hemicellulose and, in addition, the sugar composition of hemicellulose, has an important effect on the oxidation process, which is later translated into the CNF properties. This was previously observed by the authors, when significantly different rheological behavior was found depending on the selected source for TEMPO-oxidized CNF production (Serra-Parareda et al. 2021). Not only this, but the starting composition of the fibers, i.e., prior to TEMPO-mediated oxidation, has also been reported to be crucial when assessing oxidized pulps by near infrared spectroscopy, as samples can be easily clustered according to their origin (Mazega et al. 2024).

Preservation of the hemicellulose fraction plays a vital role in fiber processing due to its ability to bind with water and associate with cellulose, facilitating fiber swelling and increasing the internal porosity of the cell wall, which enhances water transport and diffusion throughout the fiber matrix. This property makes hemicellulose essential for controlling moisture content and fiber behavior in pulping and related applications (Koskela et al. 2022). The hemicellulose's composition of various monosaccharides, such as xylose, mannose, glucose, arabinose, 4-*O*-methylglucuronic acid, and galactose, will determine its hydrophilic capacity, while its amorphous structure promotes chemical accessibility. The composition and structure of hemicellulose directly affect fiber reactivity, contributing significantly to the kinetics and selectivity of the chemical reactions (Kumagai and Endo 2021). Actually, the pivotal role of hemicellulose for CNM production, particularly for cellulose nanofibers (CNFs), has been previously identified in the literature, and not only for TEMPO-mediated oxidation (Chaker et al. 2013; Lin et al. 2020; Li et al.

2021a). However, the role of hemicellulose is still unclear, and requires further investigation. Not only this, but the xylan content has also been identified to impart significant differences on CNM properties (Pääkkönen et al. 2016).

In this study, we hypothesized that the structural and chemical characteristics of the starting material strongly influence the resulting properties of CNMs when processed under identical conditions. Specifically, this work offers a comprehensive analysis of the structure–property relationships between the structural features of eucalyptus, pine, hemp, and sisal fibers and the electrostatic, physical, and rheological properties of the resulting CNMs. By highlighting the importance of selecting the appropriate starting material to achieve targeted properties and applications, this study also provides a more fundamental perspective on optimizing top-down CNM production, as it identifies pathways for improvement as a potential help for advancing the industrial adoption of this renewable, high-performance cellulose-based nanomaterial.

Experimental section

Materials

Four different commercial bleached pulps were selected: (i) eucalyptus, (ii) pine, (iii) hemp, and (iv) sisal. Eucalyptus and pine bleached kraft pulps (BKEP and BKPP, respectively) were kindly provided by LECTA group (Zaragoza, Spain), in the case of BKEP, and by Celulosa Arauco y Constitución S.A. (Los Horcones, Chile), in the case of BKPP. Hemp and sisal pulps were provided by Celulosa de Levante S.A. (Tortosa, Spain). In all cases, the pulps were provided in the form of dry laps with a moisture content around 10%. All the reagents required for TEMPO-mediated oxidation, sample processing and characterization, were acquired at Merck (Barcelona, Spain).

TEMPO-mediated oxidation

TEMPO-mediated oxidation was performed on the selected pulps using 5, 10, and 15 mmol of NaClO per gram of dry pulp, aiming at three different levels of oxidation. In all experiments, 100 mg/g of NaBr and 16 mg/g of TEMPO were dissolved in 1000 mL of deionized water. Then 15 g of dry pulp was added under gentle stirring, and the total volume was adjusted to 1500 mL. After the fibers were fully dispersed, the required NaClO was added. pH was then maintained at 10.5 by means of dropwise addition of a 0.5 M NaOH solution until no further significant changes of the pH were observed. The fibers were rinsed, filtered, and stored at 4 °C in hermetic plastic bags for further characterization and processing.

Samples were labeled by feedstock (E for eucalyptus, P for pine, H for hemp, S for sisal) and NaClO dosage (5, 10, and 15 mmol/g. For example, eucalyptus pulp treated with 5 mmol/g NaClO was labeled as E5, while hemp oxidized with 10 mmol/g NaClO was labeled as H10.

Carboxyl content determination of the oxidized pulps

The carboxyl content (CC) of the oxidized pulps was determined following a previously reported methodology (Mazega et al. 2023a). In brief, 0.5 to 2 mg of dry fiber was added to a solution containing 5 mL of methylene blue (300 mg/L) and 5 mL of borate buffer at pH 8.5. The samples were stirred and then centrifuged at 3500×*g* for 20 min. After centrifugation, 2 mL of the supernatant were transferred into a 25 mL flask containing 2.5 mL of 0.1 N HCl, and the volume was adjusted with deionized water. The absorbance at 664 nm was measured and correlated to a calibration curve.

Hemicellulose chemical composition: acidic methanolysis

Acidic methanolysis was conducted following a modified version of the protocol by Sundherg et al. (1996). In summary, 10 mg of cellulosic pulp was placed in a centrifuge vial and suspended in acidic anhydrous methanol (2 M HCl in MeOH). The suspension was heated to 100 °C using a sand-filled heating block for a duration of 4 h to ensure depolymerization. After the reaction period, the process was halted by adding 200 µL of anhydrous pyridine, followed by the introduction of 1000 µL of an internal standard solution (D-Sorbitol in anhydrous methanol, 500 mg/L).

The solvent was evaporated in a nitrogen flow, and the residue was subjected to derivatization. For this step, 200 µL of anhydrous pyridine, 200 µL of

BSTFA (with 1% TMCS), and 100 µL of TMCS were added. The derivatized sample was diluted with 500 µL of anhydrous ethyl acetate. The vials were sealed and left for sedimentation of the residue for at least 4 h. After this, the solution was transferred to a 2 mL Eppendorf tube and centrifuged at 13,200 rpm for 20 min. A 200 µL portion of the supernatant was then transferred to a GC vial for analysis.

The sugar content was measured using a gas chromatography flame ionization detector (GC-FID) system (Agilent 7890B) equipped with a DB-1701P column, ensuring accurate quantification. The process was conducted for each starting material and all the oxidized pulps.

Analytical size-exclusion chromatography (SEC)

SEC analysis was performed according to published procedures (Siller et al. 2014; Potthast et al. 2015) using a size exclusion/multi-detector (SEC-MALLS-RI) system. The system was composed of a Bio-Inert 1260 Infinity II HPLC pump (G1312B; Agilent Technologies, Waldbronn, Germany), an HP Series 1100 autosampler (G1367B; Agilent Technologies), MALLS detector (Wyatt Dawn DSP with a diode laser, λ = 488 nm, Waters Corporation) and refractive index detector (Shodex RI71, Showa Denko K.K.). Four serial SEC columns (Styragel HMW 6E Mixed Bed, 15–20 µm, 7.8 mm i.d., 300 mm length, Waters GmbH, Vienna, Austria) with one Agilent GPC guard column (PL gel, 20 µm, 7.8 mm i.d., 50 mm length; Agilent Technologies) were used as a stationary phase. As a mobile phase, *N,N*-dimethylacetamide/ lithium chloride (0.9%, w/v; filtered through a 0.02 µm filter) was used at a flow rate of 1.0 mL/min. For each measurement, a sample volume of 100 µL was injected at a 45 min run time. The molecular weight distribution (MWD) and its statistical moments were calculated based on a refractive index increment of 0.140 mL/g for cellulose in *N,N*-dimethylacetamide/lithium chloride (0.9% w/v) at 488 nm. The raw data was processed with Astra 4.73 (Wyatt Technology) and GRAMS/AI 7.0 software (Thermo Fisher Scientific).

Cellulose samples for SEC were prepared by dissolving them as described elsewhere (Potthast et al. 2015). Approximately, 12 mg of an air-dried pulp sample was disintegrated using deionized H_2O and a standard kitchen blender. The suspension was filtered using a Büchner funnel with filter paper (Lab Logistics Group GmbH, Meckenheim, Germany), washed with EtOH, and pre-dried on the filter by vacuum filtration. The sample was transferred into a 4 mL screw-cap vial and activated by shaking in 3 mL DMAc at room temperature for 16–24 h. Subsequently, the sample was filtered and dissolved in 1 mL of DMAc/LiCl (9% w/v) at room temperature. Prior to analysis, the sample was diluted with pure DMAc (0.3 mL sample solution + 0.9 mL DMAc) and filtered through a 0.45 µm syringe filter (PTFE; Agilent Technologies, Waldbronn, Germany).

X-ray diffraction

X-ray diffraction (XRD) patterns were recorded by Bruker's diffractometer D8 Advance, operating at 40 kV and 30 mA, with Cu-Kα radiation (λ = 0.1542 nm). Samples were lyophilized, ground in a domestic coffee mill (twice for 20 s) and placed on zero-diffraction silicon plates. Data were collected in reflectance mode over a 2θ range of 4.5–50°. The obtained diffractograms were fitted to Gaussian functions with Systat's PeakFit software (version 4.1.2). Baseline subtraction was set as "Linear D2" and no smoothing was applied. The distinguishable peaks of cellulose Iβ, namely those corresponding to planes (1–10), (110), (102), (200) and (004), were identified according to idealized patterns (French 2014). The crystallinity index (CI) was estimated as the ratio between the areas of the so-called crystalline peaks (A_{hkl}) and the total area (Park et al. 2010):

$$CI = \frac{A_{1-10} + A_{110} + A_{102} + A_{200} + A_{004}}{A_{total}} \quad (1)$$

The crystallite size (D) can be estimated for cellulosic samples from their XRD patterns, selecting the diffraction peak associated with a given (hkl) plane. The Scherrer's equation adopts the form (Agarwal et al. 2017):

$$D_{hkl} = \frac{0.94\lambda}{\beta cos\theta} \quad (2)$$

where β is the full width at half maximum of a diffraction peak in radians and θ is the Bragg angle that corresponds to the center of the same peak.

Solid-state nuclear magnetic resonance

Solid-state ^{13}C cross-polarization/magic angle spinning (CP/MAS) NMR spectra were obtained using a Bruker Avance III HD 400 spectrometer (Bruker, Germany), operating at a resonance frequency of 100.61 MHz. The setup featured a 4 mm dual broadband CP/MAS probe. ^{13}C spectra were recorded at 20 °C using the total sideband suppression sequence at a MAS rate of 5 kHz, a CP contact time of 2 ms and a recycle delay of 2 s. The acquisition time was 49 ms. Chemical shifts were externally referenced to the carbonyl signal of glycine at 176.03 ppm. Prior to spectral recording, samples were swollen in deionized water overnight.

All ^{13}C NMR spectra were normalized to the local maxima between 104 and 105 ppm, corresponding to the anomeric carbon of β-glucans, in OriginLab's OriginPro 8.5 software.

X-ray photoelectron spectroscopy

X-ray photoelectron spectroscopy (XPS) was carried out by means of CCiTUB's ESFOSCAN, a device based on the PHI 5000 VersaProbe 4 instrument from Physical Electronics (ULVAC-PHI). Experiments involved a monochromatic focused X-ray source (aluminum Kα, 1486.6 eV) calibrated with the 3d5/2 line of Ag with a full width at half maximum of 0.6 eV. The analyzed area was a circle of 100 µm in diameter. The resolution parameters included 27 eV of pass energy and 0.1 eV per step. Measurements took place in an ultrahigh vacuum chamber at a pressure between $5{\cdot}10^{-10}$ and $5{\cdot}10^{-9}$ Torr.

Spectra were submitted to peak deconvolution in the 280–290 eV range, corresponding to the C1s region (Yokota et al. 2021). The Voigt function was selected for multiple peak fitting in OriginLab's OriginPro 8.5 software. In general, deconvolution into three peaks (C-2/C-3, C-4/C-5/C-6, and C-1) was possible. For sisal samples, it was impossible to distinguish the C-2/C-3 peak from the C-4/C-5/C-6 one.

CNM production and characterization

All oxidized fibers underwent mechanical fibrillation via high-pressure homogenization (HPH) at a consistency of 1 wt%, following a specific pressure sequence. This sequence consisted of three passes at 300 bar followed by three passes at 600 bar.

The rheological behavior of CNM suspensions was evaluated at a consistency of 0.3 wt% (0.5 and 1% additionally for samples that did not behave like a gel at theses consistencies) using a modular compact rheometer (MCR 302e) equipped with RheoCompass software. The analysis employed a concentric cylinder (CC27) configuration and measured shear rates ranging from 0.1 to 1000 s^{-1}. The relationship between apparent viscosity and shear rate was modeled using the Ostwald-de Waele equation (Eq. 3), as previously established for CNM suspensions (Hubbe et al. 2017; Li et al. 2021b):

$$\eta = K \cdot \gamma^{n-1} \tag{3}$$

where K represents the viscosity coefficient and n is the flow behavior index. Specific spindle settings and other experimental parameters were adjusted according to the requirements of the rheometer to ensure accurate measurements.

The yield of fibrillation, expressed as the mass fraction of nanosized fibers in the CNF suspensions, was determined by centrifuging a 0.2 wt% CNM suspension at 4000×g for 30 min. The nanofibrillated fraction was expected to be contained at the supernatant, while the non-nanofibrillated fraction was assumed to be retained as sediment. The recovered sediment was oven-dried until constant weight and referred to the initial dry mass. Transmittance was determined over 0.1 wt% CNM suspensions in a Shimadzu UV-160 spectrophotometer in the wavelength range between 400 and 800 nm, using distilled water as background (Mazega et al. 2023b).

Scanning transmission electron microscopy (STEM) was conducted to assess the diluted CNM suspensions dried onto sample holders and negatively stained with uranyl acetate. The images were taken with a TESCAN CLARA at an accelerating voltage of 7 kV.

Results and discussion

The raw materials selected for the study underwent TEMPO-mediated oxidation followed by fibrillation using a high-pressure homogenizer. This process

resulted in suspensions ranging from translucent to transparent. The visual appearance of these suspensions is illustrated in Figure S1, which displays images at a consistency of 1 wt%. Notably, visual inspection alone reveals significant differences among the feedstocks, particularly regarding light scattering and viscosity. Furthermore, the severity of the oxidative process appears to influence each raw material differently, leading to intriguing transitions between low- and high-viscosity systems and variations in the water retention capacity of the resulting CNMs.

Features of oxidized CNMs

Table 1 provides the CC of the oxidized pulps as function of the selected raw material and the oxidizer amount (OA). The data reveal variations in CC depending on the fiber type, with higher CC values observed as the OA increased. Wood fibers achieved a maximum CC of approximately 1.5 mmol/g, while hemp and sisal reached slightly lower maximum values when 15 mmol of NaClO per gram of fiber was used in the TEMPO-mediated oxidation process. However, these differences are not statistically significant, and the overall trend in CC evolution was consistent across all raw materials studied. The obtained CC values are aligned with previously published results for TEMPO-mediated oxidation, indicating that all the oxidations were adequately performed (Isogai et al. 2011; Isogai and Zhou 2019; Serra et al. 2017).

Although the oxidative process appeared to have similar effects on the fibers, their properties and characteristics diverged significantly after high-pressure homogenization. For instance, the fibrillation yield for fibers oxidized at an oxidizer amount (OA) of 5 mmol/g was comparable for eucalyptus, pine, and hemp, producing nanosized fractions of approximately 42–50% by weight. However, when the OA was increased to 10 mmol/g, hemp displayed a relatively lower fibrillation yield (65.43%) compared to eucalyptus and pine, which both exceeded 70%. Notably, sisal fibers consistently exhibited the highest fibrillation yields across all conditions, outperforming the other fibers at any OA. At the maximum OA of 15 mmol/g, no sediment was observed after centrifugation for any sample, indicating nearly 100% nanofibrillation. These yields of fibrillation correlate with the transmittance of the suspensions at 0.1 wt% in the visible light range (600 nm wavelength), a correlation previously reported and attributed to the significant influence of particle size on light scattering (Puangsin et al. 2013; Signori-Iamin et al. 2022).

Table 1 Main morphological, optical and rheological features of the obtained CNMs

Feedstock	OA[a] (mmol/g)	CC (meq/g)	Yield of fibrillation (%)	T at 600 nm[b] (%)	Ostwald-de Waele regressors[c]		
					K (mPa·s^n)	n (−)	R^2
Eucalyptus	5	0.79 ± 0.04	51.16 ± 3.11	45.1 ± 0.3	1972.94	0.31	0.9822
	10	1.05 ± 0.02	73.14 ± 2.06	82.6 ± 0.2	1953.63	0.41	0.9886
	15	1.48 ± 0.07	> 95	91.0 ± 0.2	5673.35	0.39	0.9800
Pine	5	0.58 ± 0.10	43.80 ± 1.98	31.4 ± 0.1	38.97	0.60	0.9648
	10	0.96 ± 0.03	72.60 ± 4.20	78.2 ± 0.5	4025.80	0.32	0.9995
	15	1.46 ± 0.02	> 95	96.3 ± 0.4	67.11	0.72	0.9585
Hemp	5	0.60 ± 0.04	42.15 ± 1.56	37.7 ± 0.2	122.00	0.43	0.9908
	10	1.06 ± 0.01	67.26 ± 2.13	67.9 ± 0.4	3.69	1.01	0.0913*
	15	1.34 ± 0.04	> 95	88.2 ± 0.6	2.25	1.06	0.3112*
Sisal	5	0.76 ± 0.05	65.43 ± 4.07	43.1 ± 0.1	18.82	0.78	0.9866
	10	1.00 ± 0.08	91.59 ± 5.10	90.4 ± 0.3	1350.63	0.45	0.9971
	15	1.37 ± 0.04	> 95	93.7 ± 0.2	6.26	1.01	0.0214*

*Systems extremely diluted. The Ostwald-de Waele regressors at higher solid content are provided as Supplementary Material

[a]Oxidizer amount, expressed as mmol of NaClO per dry gram of fiber

[b]Transmittance of 0.1 wt% suspensions at 600 nm of wavelength

[c]All the parameters were obtained from curves at 0.3 wt% consistency

While those differences in morphological and optical properties are noteworthy, the most significant discrepancies between the CNMs from different feedstocks lie in their rheological behavior, illustrated by the Ostwald-de Waele regressors derived from the fitting to a power-law regression of the rheology curves provided in Fig. 1. These regressors correspond to diluted CNM suspensions (0.3 wt%) due to the impossibility to test all the samples at higher solid content consistently. On the one hand, some of the suspensions exhibited a thick gel-like aspect at 1 wt% consistency, requiring a plate-plate or cone-plate setup. Conversely, CNMs obtained from H10, H15 and S15 did not form gels, hindering the determination of their viscosity with this setup. On the other hand, the apparent viscosities of those samples resulting in a gel were not appropriate for their characterization with the concentric cylinders setup, requiring dilution for accurate measurements. These significant differences on the rheological behavior of the samples make their comparative assessment challenging, as 0.3 wt% results in an extremely diluted system for those samples that do not form gels at 1 wt% (H10, H15, and S15).

As displayed in Table 1 and Fig. 1, the CNM suspensions obtained from eucalyptus exhibited an increasing viscosity with the oxidation severity. This enhancement of the viscosity was relevant from 10 to 15 mmol/g of OA, increasing the consistency factor (K) from 1953.63 to 5673.36 mPa·s^n. In all cases, the eucalyptus CNMs exhibited a shear-thinning behavior, with a flow behavior index (n) lower than 1. In terms of fluid behavior, pine CNFs exhibited a similar pattern to those prepared from eucalyptus, although its maximum viscosity was found for a 10 mmol/g addition of oxidizer, together with the lowest n value

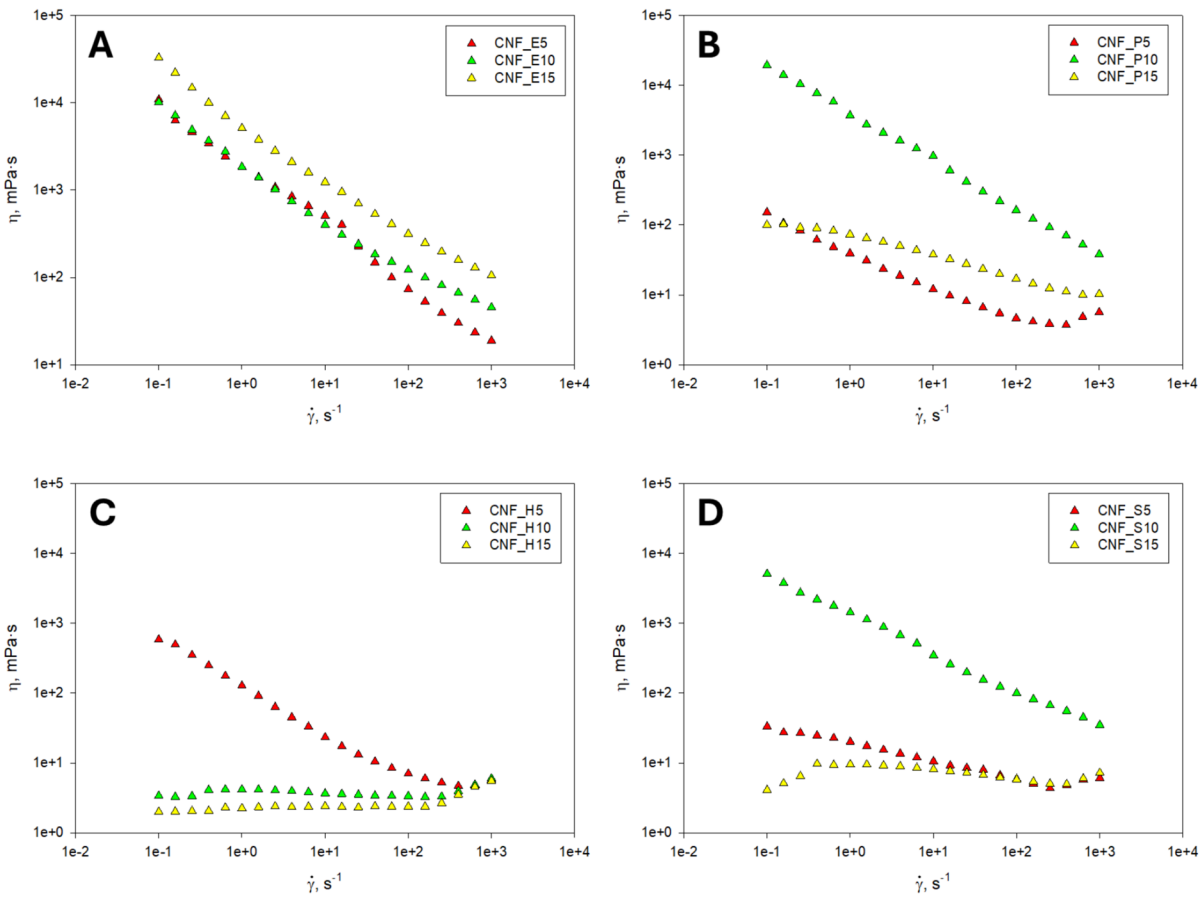

Fig. 1 Rheology curves of the obtained CNMs from eucalyptus (**A**), pine (**B**), hemp (**C**), and sisal (**D**) at different oxidation degrees

for this feedstock. This suggests that 15 mmol/g may result in an excessive OA for pine fibers that, beyond selectively oxidized C-6, may contribute to fiber degradation. TEMPO oxidation, with increasing severity, introduces carbonyl groups along the cellulose chains by oxidizing C-2 and C-3 as side reactions. Note that the selectivity of the TEMPO oxidation formally still remains very high and well above 95%. At the same time, any carbonyl group along the cellulose chain will cause immediate chain cleavage in already weakly alkaline medium according to beta-alkoxy elimination mechanisms (Hosoya et al. 2018) so that a minute amount of carbonyl structures can already affect significant chain shortening. We assume the oxidation selectivity to decrease with increasing oxidant concentrations and oxidation time. In addition, short oxidation times will primarily affect amorphous domains while longer oxidation times will increasingly oxidized also the surfaces of crystalline regions. Note that the introduction of carbonyl groups is the oxidation mode that makes monosaccharides without primary alcohol groups, such as xylopyranose in xylane, susceptible to and degradable by TEMPO oxidation. This hypothesis suggests a dynamic shift in the nature of chain degradation as oxidation advances, starting with increasing degradation of the cellulose chains as the process intensifies. The differences on the chemical composition of eucalyptus and pine have been previously reported to impart an effect over both selectivity and yield of TEMPO-mediated oxidation (Syverud et al. 2011). These differences, as it will be later discussed, may have an influence on the CNM properties, originated during the oxidation process and further highlighted upon intense fibrillation.

The CNM suspensions obtained from non-wood feedstocks, hemp and sisal, exhibited lower viscosity than those obtained from wood. This is aligned with previous studies, where nanocrystal-like structures were found for CNMs obtained from these raw materials, attributed to a lower 2D fractal dimension (Serra-Parareda et al. 2021). Nonetheless, the rheological characterization revealed that both hemp and sisal can transition from gel-like suspensions to low-viscosity fluids. This is illustrated by the fitting of the rheology curves to the Ostwald-de Waele equation, which resulted in extremely low R^2 for samples H10, H15 and S15, demonstrating the unsuitability of this model for these specific samples. According to the selected rheological model, these samples exhibited an n higher than 1, which indicates a slight shear-thickening behavior. CNF suspensions usually exhibit shear-thinning fluid characteristics ($n < 1$) due to nanofibril alignment with the flow and, in addition, thixotropic behavior (Hubbe et al. 2017). This shear-thickening behavior could be explained by an excessive dilution of the system for these samples, where water may impart most of the effects on the viscosity measurements, with a residual role of the CNFs present in the suspension. We cannot exclude that the higher amount of carbonyl structures introduced at high oxidation degrees influences the rheological behavior by dynamic interchain crosslinking of the hemiacetal/hemiketal type. It should be noted that carbonyl structures in oxidized celluloses (and polysaccharides in general) are not present in their usual sp^2-hybrid form as C=O, but as masked carbonyl moieties with sß3-hybrid carbonys (hydrates, hemiacetals, hemiketals, hemialdals). Actually, the rheological power-law model cannot capture Newtonian viscosity plateaus, found at both extremely low and high shear rates of CNF suspensions (Lasseuguette et al. 2008). The extreme dilution of the CNM suspensions led to a plateau on viscosity for all the shear rate range (Fig. 1C, D), making the fitting of the power-law model unsuitable for these samples. The dilution effect over the unsuitability of the power-law model was confirmed assessing the specific samples from hemp and sisal, at 1 wt% consistency (Figure S2). The Ostwald-de Waele regressors for these samples at 1 wt% consistency are provided in Table S1. As expected, at increasing consistency, the rheological behavior of these samples exhibited shear-thinning characteristics with an improved fitting to the power-law model, corroborating the negative effects of excessive dilution.

Figure 2 presents STEM images of negatively stained CNMs, previously dried onto sample holders from a diluted suspension. Specifically, Fig. 2a, b reveal eucalyptus and pine CNFs obtained through oxidation with 10 mmol of NaClO. Both samples exhibit an entangled network of kinked nanosized fibrils with a high aspect ratio. This network appears more pronounced in the pine sample compared to the eucalyptus one, being consistent with their rheological behavior. Notably, the K factor of P10 CNFs accounted for 4025.80 $mPa{\cdot}s^n$, while E10 CNFs yielded a K factor of 1953.63 $mPa{\cdot}s^n$. Additionally, the shear-thinning behavior was more pronounced in

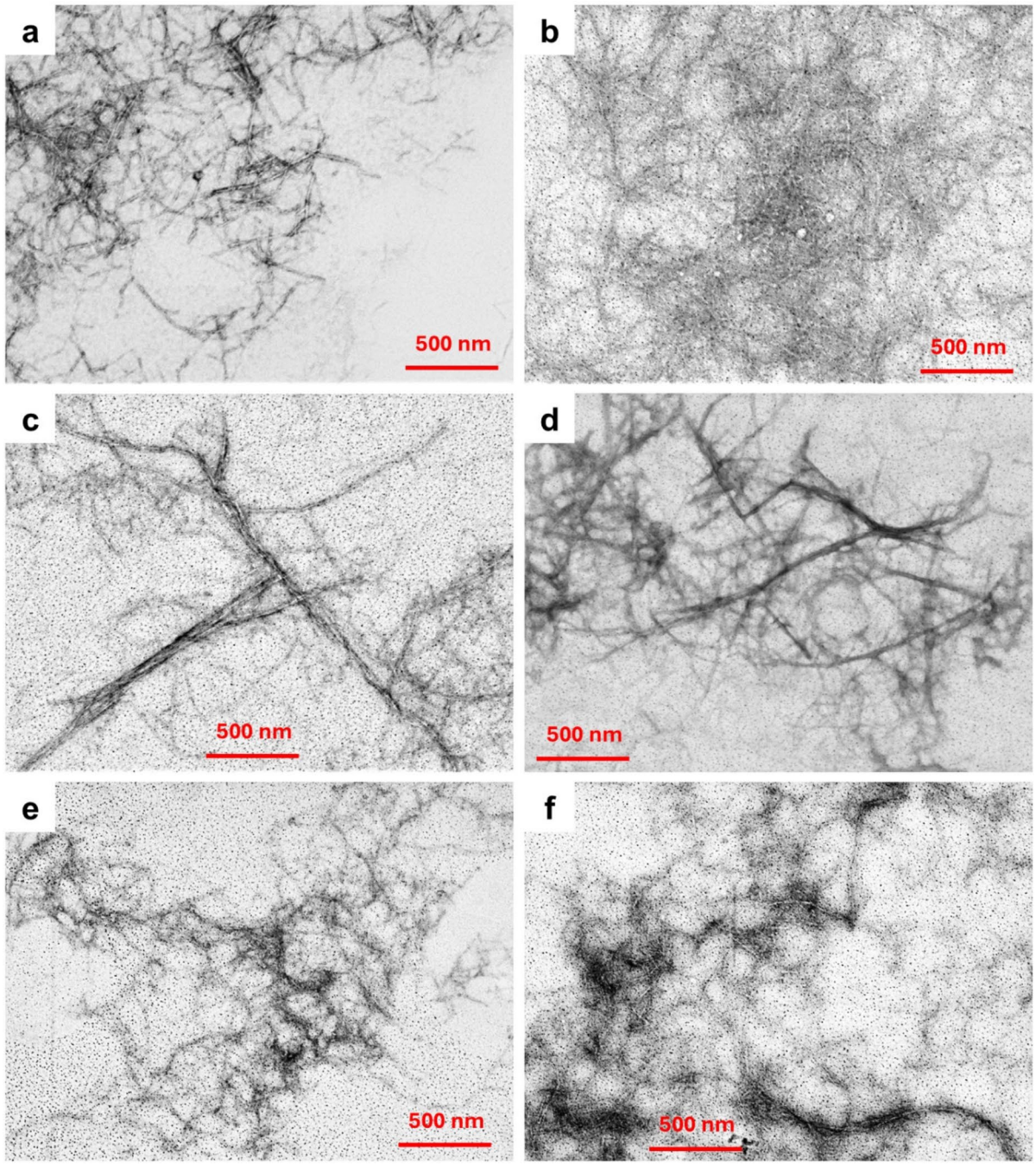

Fig. 2 STEM images of diluted CNM suspensions of E10 (**a**), P10 (**b**), H5 (**c**), H10 (**d**), S5 (**e**), and S10 (**f**)

P10 CNFs than in E10 CNFs. The fibrillar, network-like structure observed in the STEM images supports the rheology curves, further confirming their classification as CNFs and their gel-forming capacity at low concentration.

Figure 2c, d provide a STEM image of CNMs obtained from H5 and H10, respectively. In both cases, the samples exhibited long structures that, at the same time, exhibited a significantly greater diameter than those corresponding to eucalyptus and pine.

Additionally, these bigger fibers show a relatively low entanglement, which prevents the formation of a strong network and, thus, resulting in low-viscosity suspensions. Remarkably, the presence of bigger structures, although at the nanoscale, supports the lower transmittance of the obtained suspensions compared to those prepared from eucalyptus, pine, and sisal, as revealed in Table 1. These differences are particularly patent with the addition of 10 mmol/g of NaClO, where the transmittance is significantly lower in the case of hemp CNMs. Finally, Fig. 2e, f provide images of S5 and S10, respectively, where the formation of networks becomes apparent. Particularly, the entanglement appears to be higher in the case of S10 CNFs (Fig. 2f) than in the case of S5 CNFs (Fig. 2e), although the entanglement degree is somewhat difficult to quantify. In any case, this is supported by the rheology provided in Fig. 1 and the values of the Ostwald-de Waele parameters, where a shear-thinning behavior was found for both samples, suggesting this network forming capacity and their alignment with the flow when subjected to shear stress.

Chemical changes on TEMPO-oxidized fibers and sugar composition of methanolysates

The discrepancies in CNM properties across raw materials can be attributed to their inherent differences, including chemical composition and structural characteristics, such as crystallinity or distribution of molecular weights, which are closely related to fiber recalcitrance and, thus, accessibility. While differences in chemical composition readily explain the variations observed in eucalyptus and sisal, they do not fully account for the similarities between pine and hemp. Previous studies determined the chemical composition of these materials, revealing that pine pulp comprises 87.4% cellulose and 7.4% hemicellulose, closely resembling hemp, which contains 86.5% cellulose and 7.1% hemicellulose. In contrast, eucalyptus has a higher hemicellulose content (17.5%), while sisal exhibits less (13.7%) (Aguado et al. 2022; Sanchez-Salvador et al. 2022). Additionally, the MWD highlighted differences among eucalyptus, sisal, and the other materials, while revealing strong similarities between pine and hemp, as revealed in Fig. 3.

As reflected in Table 2, eucalyptus fibers exhibited the largest average molecular weight, accounting for 414.35 kDa (M_w), while sisal fibers exhibited

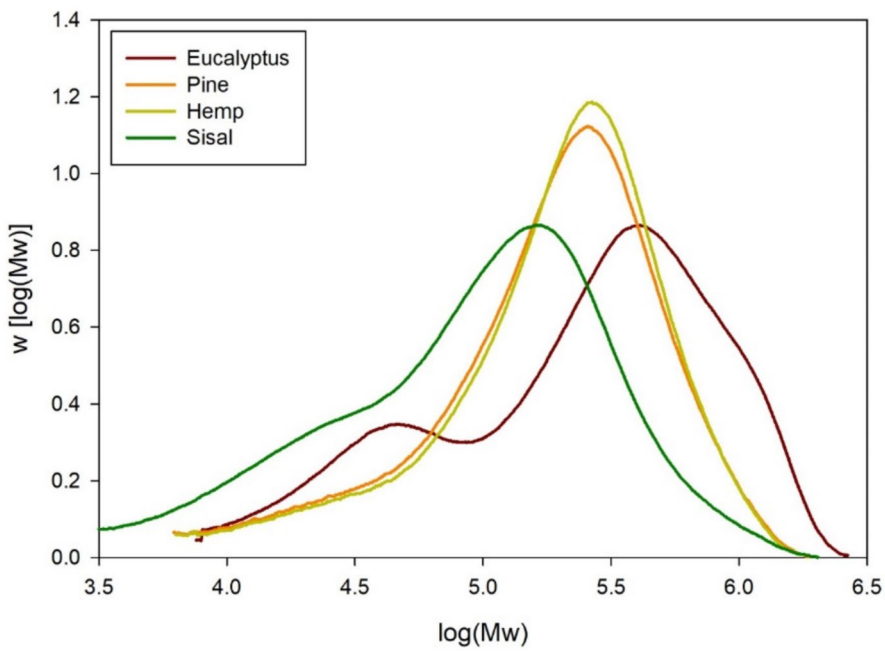

Fig. 3 Molecular weight distribution (MWD) of the starting materials

Table 2 Molecular weight averages (weighted in number, weight, and Z-average) and dispersity in the four materials of study

Feedstock	M_n (kDa)	M_w (kDa)	M_z (kDa)	Đ
Eucalyptus	92.34	414.35	812.50	4.50
Pine	90.46	272.10	478.75	3.01
Hemp	99.99	279.20	471.80	2.81
Sisal	38.77	168.25	399.20	4.34

the lowest (168.25 kDa for M_w). The molecular weight distribution determined by GPC comprises all contained polysaccharides, both from amorphous and crystalline domains, linear and branched, i.e., cellulose and hemicelluloses. In line with the chemical composition, pine and hemp exhibited a similar MWD and average values, as well as dispersity (Đ).

These differences in cellulose and hemicellulose content, and in MWD, however, provide limited insight into the variations between the CNMs derived from pine and hemp. The differences on the MWD between eucalyptus and sisal may also originate in the different hemicellulose content, which cannot be evaluated by viscosimetry analysis. This was previously noted in a study employing near-infrared (NIR) spectroscopy to quantify the carboxyl content (CC) of TEMPO-oxidized fibers, where principal component and linear discriminant analyses (PCA-LDA) revealed overlap between pine and hemp (Mazega et al. 2024). One plausible explanation lies in differences in sugar composition, which influences the outcome of TEMPO-mediated oxidation and, consequently, the properties of the resulting CNMs. The dominating monosaccharides of the galactoglucomannans in pine are hexoses which all have a TEMPO-oxidizable C-6, while the dominating monosaccharides in the arabinoxylan of hemp are pentoses which lack this primary alcohol unit. Exemplarily, Syverud et al., (2011) similarly highlighted the impact of sugar composition differences, particularly between eucalyptus and pine, on the characteristics of TEMPO-oxidized CNFs. Also here, the reactivity difference between pentoses and hexoses explains the observations. In this sense, the neat and TEMPO-oxidized fibers were subjected to a methanolysis process in order to quantify the sugar composition within the hemicellulose fraction of each starting material for CNM production. Results, consisting of glucose, xylose, mannose and galactose contents, are provided in Fig. 4.

Considering the evolution of the different sugar composition at increasing CC—corresponding to oxidation severity—for each feedstock, together with the observed features of the different CNFs, it becomes apparent that xylan content, quantified as xylose (Fig. 4B), may have a determining role on the effect of TEMPO-mediated oxidation. Xylan, primarily located at the surface and distributed along the outer layer of the secondary wall (S2), with its amorphous structure and abundance of hydroxy groups, is more hydrophilic than cellulose (Pääkkönen et al. 2016). Its inherently outward-oriented conformation hinders the formation of a densely packed fiber structure, creating more space between cellulose fibers (Arola et al. 2013). This spatial arrangement within the fiber matrix allows for increased water affinity and facilitates accessibility, making the fibers more susceptible to chemical interactions (Sanchez-Salvador et al. 2022; Gupta et al. 2023). This higher accessibility is particularly apparent at low oxidation degrees, where both eucalyptus and sisal CNFs already exhibited a gel-like behavior, proving enhanced colloidal stability and water uptake, while this was not observed for pine and hemp (i.e. 5 mmol/g of OA) (Rodionova et al. 2013). Note that among the hemicellulose polysaccharides and resulting monosaccharides involved (see Fig. 4), xylopyranose is the only one that is formally inert to TEMPO oxidation (no primary hydroxy group) while all hexopyranoses (from glucose, mannose and galactose) can be readily oxidized. It is hypothesized that the higher accessibility provided by the hemicellulose structure prevents much of the internal fibrillation typically caused by oxidative cleavage of cellulose chains. This process becomes more evident as the fiber surface becomes predominantly oxidized, with the oxidation degree increasing at a similar rate as fiber degradation, thereby exposing additional surface for selective C-6 oxidation. As the exposed surface reaches a stage where most of its C-6 sites are oxidized, the reaction is expected to shift again towards side reactions (chain degradation), driven by the introduced carbonyl groups. This creates a limiting effect, whereby an increase in oxidative power no longer results in additional surface oxidation due to the degradation of oxidized fibers, which become increasingly susceptible due the harsh reaction conditions. Pääkkönen et al., (2016) highlighted

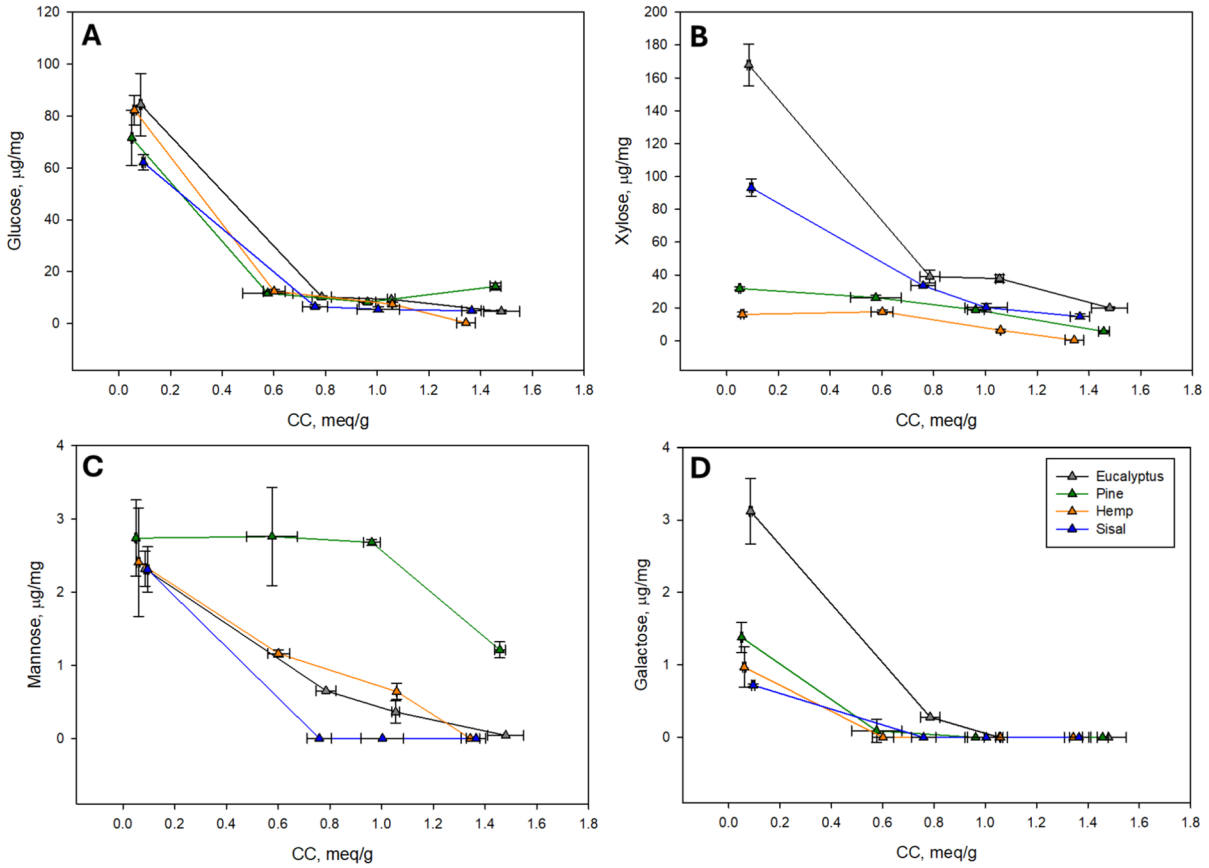

Fig. 4 Evolution of the glucose (**A**), xylose (**B**), mannose (**C**), and galactose (**D**) contents as function of the carboxyl content (CC) for each starting material

the importance of xylan on the swelling and processing characteristics of TEMPO-oxidized CNFs, indicating the relevance of appropriately selecting the raw material prior to oxidation and fibrillation for the production of CNFs. Actually, Sang et al., (2017) reported that the amorphous regions of fibers are degraded first, generating dissolved fragments of cellulose. This has been supported by other authors, which hypothesized that the specific surface of cellulose could be enlarged due to the degradation of these small fragments, exposing more primary hydroxy groups to be oxidized (Isogai et al. 2009; Shibata & Isogai 2003; Zhou et al. 2008).

Although the chemical composition of the starting materials, as well as their evolution with oxidation, can provide some interesting insights on the differences between the obtained CNFs and their rheological behavior, there might be other aspects influencing this variety of both morphological and rheological features. On the one hand, pine and hemp share a relatively low xylan content, while the characteristics of the CNMs are significantly different, particularly in terms of rheology. On the other hand, while sisal exhibits a similar behavior than eucalyptus at low oxidation degrees, the viscosity of CNM suspensions experiences a significant drop at high oxidation rates. The low viscosity could be attributed to depolymerization during the oxidative process, which is known to drastically reduce the chain length, translating into fiber degradation (Hosoya et al. 2018).

Insights from X-ray diffraction

As it can be seen from Fig. 5, diffractions on (110) and (1–10) planes, located between $2\theta = 14.1°$ and $2\theta = 16.6°$, were hardly distinguishable from each

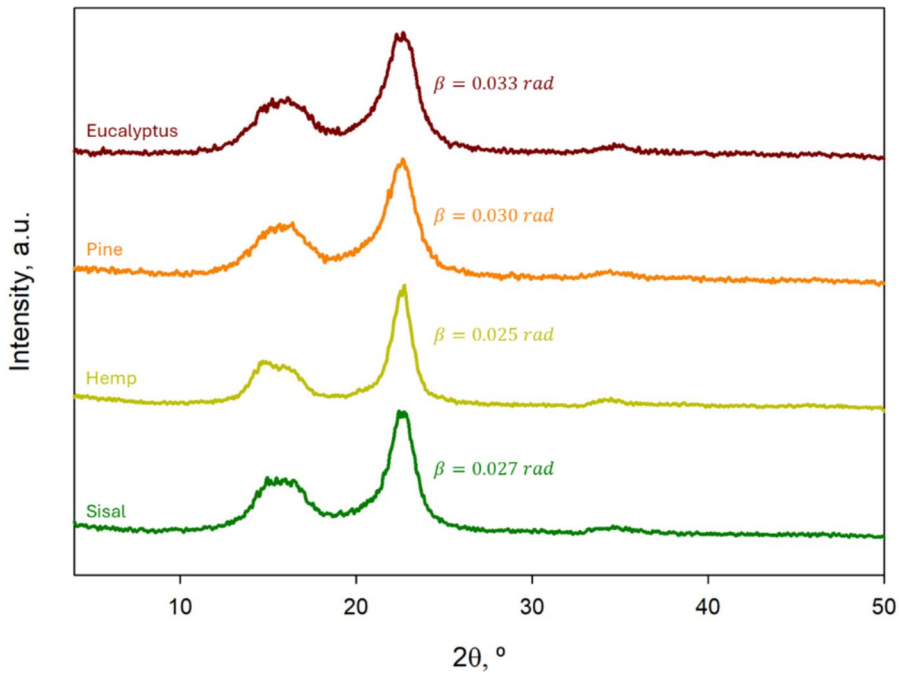

Fig. 5. 1D XRD patterns recorded for the non-oxidized starting materials. The full width at half maximum of the (200) peak is displayed for each of the profiles

Table 3 Crystallite size for the different starting materials and crystallinity as a function of OA

Starting material	D_{200} (nm)	CI			
		Non-oxidized	5 mmol/g	10 mmol/g	15 mmol/g
Eucalyptus	4.48	0.58	0.64	0.68	0.75
Pine	4.93	0.61	0.64	0.68	0.78
Hemp	5.92	0.78	0.85	0.87	0.89
Sisal	5.47	0.69	0.73	0.76	0.77

other, as commonly found among natural samples (Nam et al. 2016). In contrast, the (200) diffraction peak was consistently clear, with little and identifiable overlapping from the (102) diffraction. Hence, the prominent (200) peak, at $2\theta \sim 22.5°$, has been used for the calculation of D. In Table 3, this result is shown along with CI values for the different OA studied. The deconvolution is depicted in Figure S3, while Table S2 presents the amplitude and area of the fitted crystalline peaks.

The width of the (200) diffraction peak was higher for wood-sourced cellulose than for cellulose from annual plants: $\beta_{eucalyptus} > \beta_{pine} > \beta_{sisal} > \beta_{hemp}$ (Fig. 5). Subsequently, D_{200} followed the reverse order (Table 3). The slightly higher crystallite size in non-wood materials explains their failure to reach CC values of 1.5 mmol/g. Given the spatioselective nature of the reaction, only the surface of elementary fibrils was oxidized, whilst inner cellulose chains remained chemically unavailable (Wang et al. 2025). In another context, the tight packing of cellulose chains in fibrils from hemp and sisal, associated with their relatively high CI, was one of the causes for their lower viscosity at a given shear rate. Likewise, their lack of an abrupt shear-thinning behavior can be related to a stiffer, more crystalline structure, which conditioned the response of the fibrillar network to deformation in aqueous suspension (Li et al. 2015).

Oxidation selectivity towards hydrated domains also explains the apparent increase in CI with OA. Although the classical two-phase model for cellulose often leads to oversimplifications, it is useful to describe the preferential oxidative cleavage of the most reactive parts, *i.e.*, the so-called amorphous fraction. Consistent with our current understanding of cellulose crystallinity (Chami Khazraji and

Robert 2013; O'Neill et al. 2017; Chen et al. 2022), the amorphous fraction is constituted by those macromolecules or units thereof that, instead of displaying maximum hydrogen bonding to adjacent carbohydrate chains, are more accessible to water. This includes not only a portion of cellulose, but also most of hemicellulose, including heteropolysaccharides, such as xylans and glucomannans (Table 3). As the degree of oxidation increased, all pulps exhibited a steady increase in crystallinity, mainly due to the removal of water-solvated, partly oxidized cellulose and, in general, hemicellulose. No significant effects were observed on peak width, but simultaneously tracking CI and D with one-dimensional XRD patterns is hindered by their interrelations. As French (2022) noted, a cellulosic sample consisting of few large crystallites will seem (and, in fact, can be deemed) more crystalline than another sample composed of many small crystallites. In this case, given that recrystallization or crystal nucleation phenomena were not possible under the experimental conditions of this study (Naduparambath et al. 2018), the increase in CI was only due to the partial solubilization of amorphous parts of the starting material.

Investigating reaction effects through solid-state NMR and XPS

All ^{13}C NMR spectra showed the carbon peaks common to native β-glucans (Fig. 6). From lower to higher field, these signals and the approximate chemical shift for their maxima are: C-1, the anomeric carbon, at 104.4–104.9 ppm; C-4, split into that of inner chains at 88.2 – 88.5 ppm (crystalline) and that of

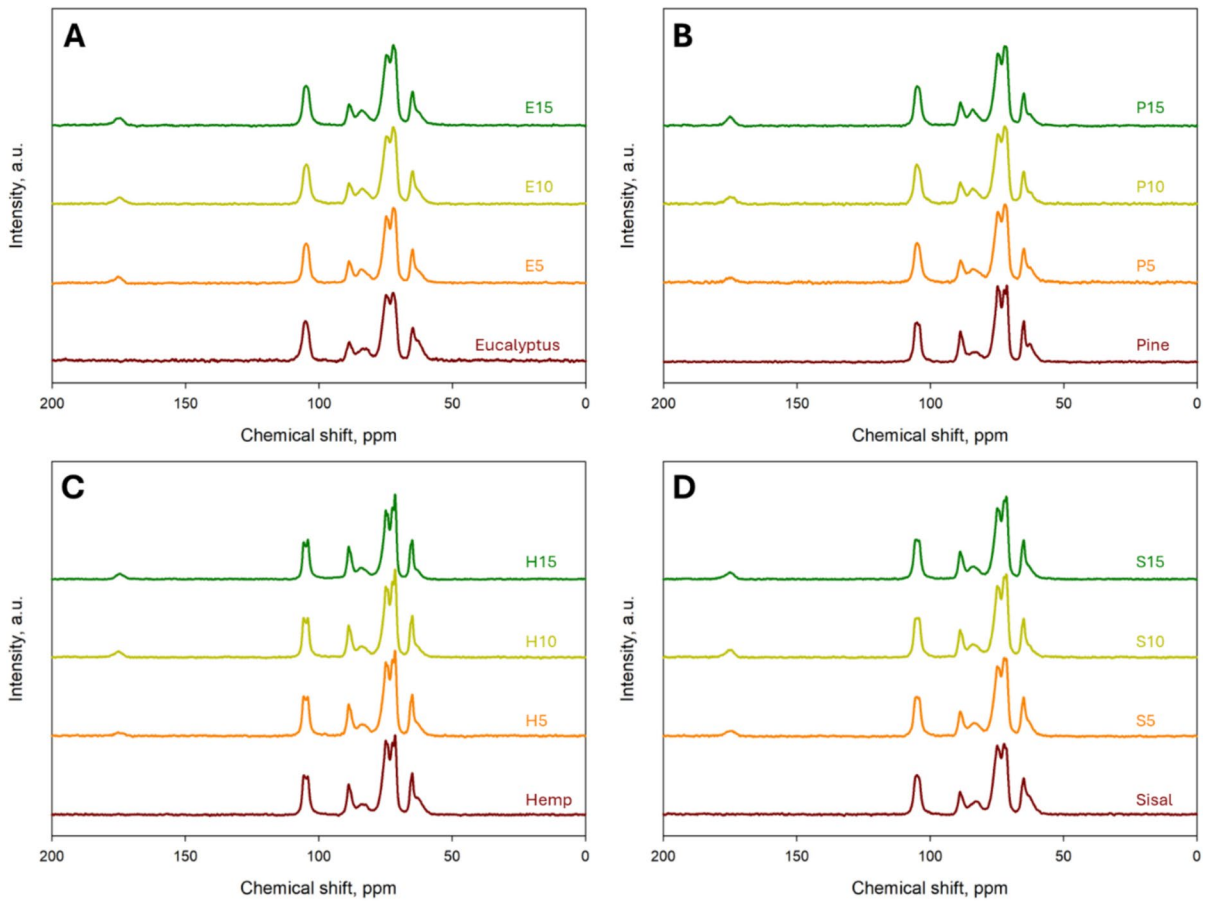

Fig. 6. ^{13}C NMR spectra of non-oxidized and TEMPO-oxidized fibers at different OA for eucalyptus (**A**), pine (**B**), hemp (**C**), and sisal (**D**). All intensity values have been normalized with respect to the C-1 peak (104.4–104.9 ppm)

outer chains at 83.5–84.3 ppm (exposed); C-2, C-3 and C-5, appearing overlapped as a pseudo-doublet at ~72.2 and ~75.0 ppm; C-6, split into that of inner chains at 64.7–64.9 ppm and that of outer chains at 62.8 – 63.3 ppm. Regardless of the raw material, TEMPO-mediated oxidation produced the progressive decrease of the resonance of outer C-6, the peak located most upfield, and the appearance of a carboxyl carbon signal at 174.4–174.7 ppm (Tang et al. 2024).

The spatioselective nature of the reaction is precisely corroborated by the relative reduction of outer C-6 signals (with respect to the C-1 peak). In contrast, the resonance peaks for C-6 of inner chains were either unaltered or slightly increased. Another noticeable effect of oxidation was the ~0.5 ppm shifts downfield of outer C-4 signals, due to the increasing percentage of neighboring C-6 carboxyls. Finally, the upfield part of C-2/C-3/C-5 pseudo-doublets increased in relative area and intensity, but without influence on the total area of double peaks. This can be easily explained by the shielding of C-5 carbons by the neighboring carboxyl groups in oxidized units, causing a shift upfield. Spectra offer no evidence on β-elimination products (Hosoya et al. 2018), as their concentration—similar to the concentration of introduced carbonyl groups—is too small for NMR detection, although the effect on the molecular weight loss was evident.

Regarding differences among starting materials, some unique features were displayed by hemp fibers: the C-1 NMR signal was found split as a doublet and a sharp peak appeared at 72.2 ppm (C-2). Despite the apparent peculiarity of such a profile, it matches other CP/MAS ^{13}C NMR spectra of pure cellulose I samples (Kono et al. 2002).

While ^{13}C NMR spectroscopy analyzed the whole volume of the sample in each case, XPS analyses

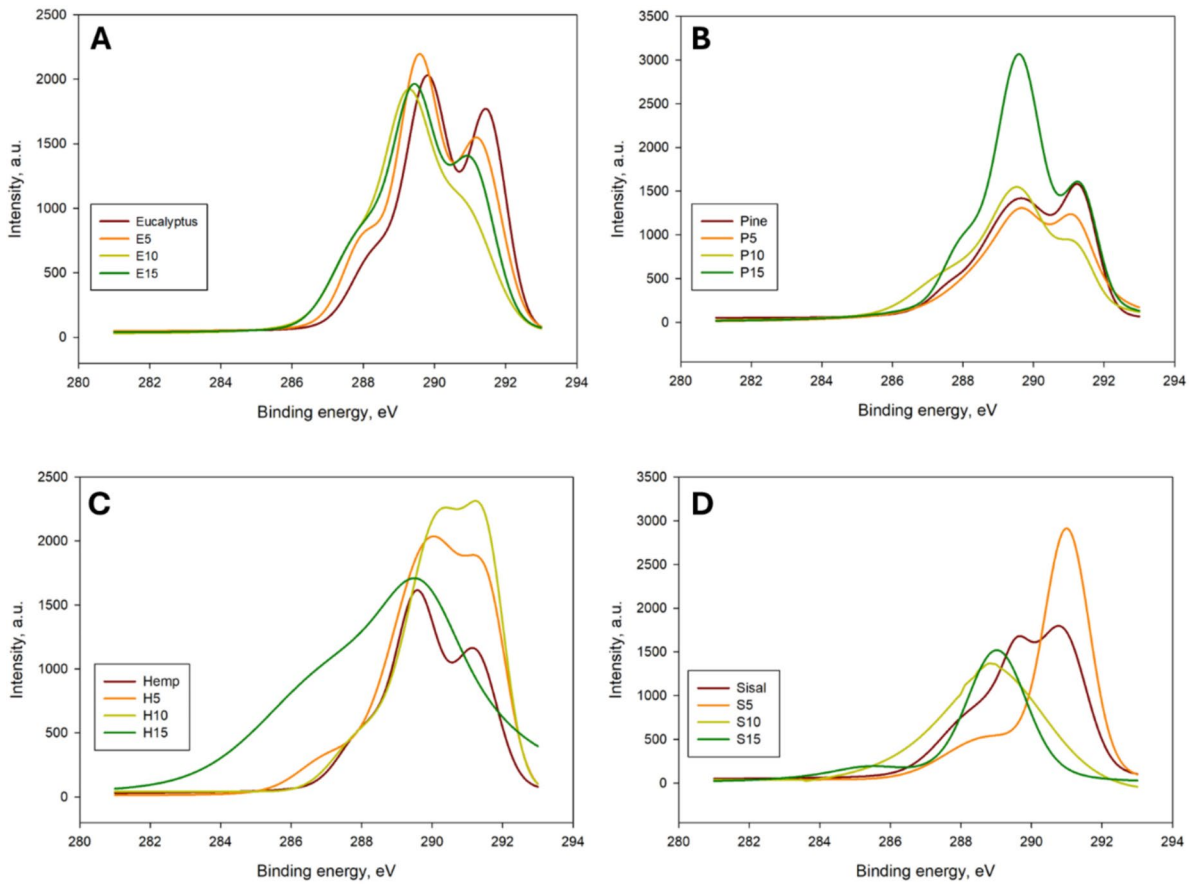

Fig. 7 X-ray photoelectron spectra for samples from eucalyptus wood (**A**), pine wood (**B**), hemp (**C**), and sisal (**D**)

provide specific information on surface chemistry (Fig. 7, Figure S4). As a drawback, the identification of specific carbon atoms is not straightforward. The most frequent approach involves a three-peak deconvolution that corresponds, in increasing energy order, to C–C/C–H, C–O, and O–C–O/C = O (Stevens and Schroeder 2009; Aiello et al. 2024). In other words, the higher the electron density on carbon, the lower the binding energy. Nonetheless, Kostov et al. (2018) associated each of the carbon atoms of anhydroglucose units to specific binding energies: C-2/C-3 < C-4/C-5/C-6 < C-1.

Among non-oxidized fibers, the surface of those from eucalyptus had the highest relative area associated to O–C–O/C = O, specifically 17.7% of total C1s area (Table S3). This includes the contribution from glucuronoxylan, and more particularly from its ester groups and glucuronic acid units (Gupta et al. 2023). In hemp, with a small hemicellulose fraction, the area of the higher-energy peak following deconvolution accounted for 9.2%. Another question to consider is, beyond the unit cell of cellulose Iβ, the habit or shape acquired by the transversal section of cellulose microfibrils, as there is still uncertainty about the positioning of outer cellulose chains (Cosgrove et al. 2024). Be it due to a different arrangement of external glucan chains or to a different hemicellulose allocation, the overall electron density on the surface of hemp fibers can be deemed higher.

Moreover, differences were accentuated by oxidation. Spectra for wood fibers kept the same qualitative profile, regardless of the oxidation degree. In quantitative terms, the reaction had mixed effects on relative areas, given the co-existence of depolymerization (loss of O–C–O), oxidation (gain of C = O), and removal of hemicellulose (loss of both O–C–O and minor C = O). Carbonyl groups introduced at C-2 or C-3 as a result of incomplete oxidation selectivity are present in masked form (see above) and would appear as O–C–O (sp^3 carbon) rather than C = O (sp^2 carbon). In the case of non-wood materials, the reaction produced shifts towards lower binding energy. This is especially noticeable in the spectra of hemp with OA = 15 mmol/g, where peak broadening was also observed, and those of sisal with OA = 10 mmol/g or OA = 15 mmol/g (Fig. 7). It may be concluded that the surface of annual plant fibers was degraded to a greater extent during the reaction, in comparison with their woody counterparts.

On structure–property relationships

Understanding how the molecular and supramolecular structure of the raw material can affect the properties of CNMs obtained thereof is extremely helpful for popularizing the large-scale production of nanocellulose. Most of the properties summarized in Table 1, namely the content in carboxyl groups, the yield of nanofibrillation and the transparency, displayed similar values. The differences found in these properties can be satisfactorily explained by structural results. For instance, fibers from annual plants reached a slightly lower maximum CC than wood pulp fibers because the former had less chemically accessible carbohydrate chains than the latter, *i.e.*, larger crystallites. However, the rheological behavior of CNM aqueous suspensions differed not only quantitatively, in a matter of orders of magnitude, but also qualitatively, with the raw material. Specifically, the consistency index in dilute aqueous suspensions of highly oxidized CNFs (0.3 wt%) lied above 1 $Pa{\cdot}s^n$ when the source was eucalyptus wood, but below 10 $mPa{\cdot}s^n$ if the feedstock was hemp. In addition, while dilute CNF suspensions from both eucalyptus and pine clearly showed shear-thinning behavior ($n < 1$), this was not observed for CNFs from hemp or sisal with high oxidation degree. Although increasing CNF concentration to 1.0 wt% attained flow behavior indices of 0.56 – 0.62 for hemp and sisal with OA = 15 mmol/g (Table S1), viscosity remained much lower than that of CNFs from wood pulps. All in all, the rheological behavior of CNFs from annual plants approached that of CNCs (Qiao et al. 2016; Serra-Parareda et al. 2021). In dilute suspensions, CNFs adopted a high degree of alignment with the flow, *i.e.*, nearly isotropic orientations.

Establishing structure–property relationships between the starting cellulosic fibers and the rheological behavior of the resulting nanocellulose suspensions is a complex task. In all cases, fibers mostly consisted of cellulose Iβ (Fig. 5), little difference was found between the average molecular weight of hemp carbohydrates and that of pine carbohydrates (Fig. 3), and both sources had low xylan content (Fig. 4). In addition, effects of TEMPO-mediated oxidation on the chemical composition were rather similar, as shown by ^{13}C NMR (Fig. 6). Perhaps highlighting key differences, XPS showed shifts towards lower binding energy in the case of

non-wood materials, which were accentuated by oxidation (Fig. 7). However, despite the knowledge on the positioning of the inner chains of the different cellulose polymorphs (French 2014), more research is needed to characterize the topology of the microfibril surface for different raw materials (Cosgrove et al. 2024).

For woody CNF suspensions, the increase in viscosity for a given shear rate is related to the amount of water whose translational and rotational freedom is restricted (Aguado et al. 2023). Electroviscous effects from carboxylate groups and a high availability of hydrophilic surfaces contribute to such restrictions. In this context, the positioning of hemicelluloses, especially xylan, on the surface of cellulose microfibrils plays an essential role. Xylan-attached fibrils are intrinsically more hydrated, with more than half of xylan's H-bonding capabilities being dedicated to water (Pääkkönen et al. 2016). In turn, the outer cellulose chains in each crystallite (or elementary fibril) are initially less accessible to degradation by ClO^- and BrO^- ions. The stronger thickening effects of eucalyptus CNFs, compared to pine CNFs, are partially due to the sacrificial protective role of xylan.

Hillscher et al. (2024) discussed that effects of TEMPO-mediated oxidation on the physical properties of oxycellulose are closely related to the chemical composition of the fiber prior and after the reaction. Chemical accessibility plays a crucial role, since the initially low proportion of surface primary hydroxy groups exposed to the reaction medium will hinder the oxidation rate. As the original structure of the fiber suffers progressive degradation, more surface –OH groups are exposed, reaching higher substitution on the C-6 position. Introduced carbonyl group along the cellulose chain tend to undergo extensive formation of dynamic interchain hemiacetal/hemiketal linkages. In parallel, as depolymerization occurs, it does so in irregular ways through the fibrils (Ono et al. 2021). Depolymerization decreases the capabilities of CNFs to catch water by reducing the aspect ratio and, thus, their capacity to generate entangled networks (Batchelor 1970). A higher rate of degradation in the case of annual plant-sourced fibers was likely a major cause for the low consistency index of the resulting CNF suspensions.

Conclusions

Despite the similarities among different lignocellulosic feedstocks in terms of chemical composition, supramolecular structure, and average molecular weight, oxidized CNMs produced thereof present striking differences. The most remarkable one lies in rheology, despite an identical CNM production procedure. On one hand, eucalyptus-sourced CNM suspensions were highly viscous at a given shear rate and, even if diluted, consistently displayed a shear-thinning behavior. This is indicative of cellulose nanofiber (CNF) like structure, which was supported by the obtained STEM images. Pine also revealed this CNF-like behavior, exhibiting an entangled network even at highly diluted states. On the other, non-wood CNFs, especially those from hemp, approached a behavior more typically associated with CNCs in dilute aqueous suspensions. This effect was also observed for sisal at high oxidation degrees. This study does not attribute this difference to a single feature, but to the additive and superimposing contribution of significant differences in multiple characteristics. Specifically, hemp fibers contain much less xylan (acid methanolysis), their cellulose Iβ crystallites are larger (XRD), their fibril surface has higher overall electron density (XPS), and they are more easily degraded during TEMPO-mediated oxidation. The present study highlighted the importance of feedstock selection for CNM production, especially if their planned application involves thickening effects. For that, factors contributing to higher viscosity, such as a high hemicellulose content (especially xylan), a small crystallite size, a relative electron deficit on surface carbons atoms, and a high average molecular weight, should be enforced. Additionally, the present work provides insight into the appropriate selection of the starting material based on the intended application, demonstrating that CNMs can achieve similar surface charges despite exhibiting distinct rheological behaviors. Furthermore, the evolving rheological properties of certain starting materials, such as hemp and sisal, enable the implementation of cascade-like processes, with side-extractions at varying oxidation levels. The present work, beyond elucidating structure-process-property relationships for CNM production, highlights the need for further research to facilitate the full industrial deployment of CNMs.

Acknowledgments Authors wish to acknowledge the financial support of the agencies listed in the Funding section. André Mazega acknowledges the University of Girona for the financial support to the mobility action to BOKU within the IFMOB program. The support by the Austrian Biorefinery Center Tulln (ABCT-II) is gratefully acknowledged. The authors also thank Dr. Markus Bacher and Dr. Sonja Schiehser for their invaluable assistance with solid-state NMR and GPC, respectively. Marc Delgado-Aguilar is a Serra Húnter Fellow.

Author contribution A.M.: Investigation; Writing – Original Draft; Funding acquisition; A.F.L.: Investigation; Data Curation; Visualization; R.J.A.: Investigation; Formal analysis; Writing – Original Draft; A.P.: Visualization; Resources; R.M.: Methodology; Validation; T.R.: Writing – Review & Editing; Resources; Supervision: M.D.-A.: Conceptualization; Funding acquisition; Methodology; Writing – Review & Editing; Supervision; Project administration.

Funding Open Access funding provided thanks to the CRUE-CSIC agreement with Springer Nature. Open Access funding provided thanks to the CRUE-CSIC agreement with Springer Nature. This research received funding from the Spanish Ministry of Science, Innovation and Universities (ArtInNano, CNS2022-135789), and the University of Girona and Banco Santander (IFUdG2020).

Data availability Data can be made available upon request to the corresponding author.

Declarations

Competing interest The authors declare no competing interests.

Ethical approval Not applicable.

References

Agarwal UP, Ralph SA, Baez C et al (2017) Effect of sample moisture content on XRD-estimated cellulose crystallinity index and crystallite size. Cellulose 24:1971–1984. https://doi.org/10.1007/s10570-017-1259-0

Aguado R, Tarrés Q, Pèlach MÀ et al (2022) Micro- and nanofibrillated cellulose from annual plant-sourced fibers: comparison between enzymatic hydrolysis and mechanical refining. Nanomaterials 12:1612. https://doi.org/10.3390/nano12091612

Aguado RJ, Mazega A, Tarrés Q, Delgado-Aguilar M (2023) The role of electrostatic interactions of anionic and cationic cellulose derivatives for industrial applications: a critical review. Ind Crops Prod 201:116898. https://doi.org/10.1016/j.indcrop.2023.116898

Aiello A, Nguyen HG, Stafford CM, Woodcock JW (2024) Impact of coagulation solvent interactions on porous morphology evolution in cellulose xerogels. Carbohydr Polym 323:121454. https://doi.org/10.1016/j.carbpol.2023.121454

Alila S, Besbes I, Vilar MR et al (2013) Non-woody plants as raw materials for production of microfibrillated cellulose (MFC): a comparative study. Ind Crops Prod 41:250–259. https://doi.org/10.1016/j.indcrop.2012.04.028

Aracri E, Vidal T, Ragauskas AJ (2011) Wet strength development in sisal cellulose fibers by effect of a laccase–TEMPO treatment. Carbohydr Polym 84:1384–1390. https://doi.org/10.1016/j.carbpol.2011.01.046

Arola S, Malho JM, Laaksonen P et al (2013) The role of hemicellulose in nanofibrillated cellulose networks. Soft Matter 9:1319–1326. https://doi.org/10.1039/c2sm26932e

Balea A, Fuente E, Monte MC et al (2020) Industrial application of nanocelluloses in papermaking: a review of challenges, technical solutions, and market perspectives. Molecules 25:526. https://doi.org/10.3390/molecules25030526

Batchelor G (1970) Slender-body theory for particles of arbitrary cross-section in Stokes flow. J Fluid Mech 44:419–440

Bettaieb F, Khiari R, Hassan ML et al (2015) Preparation and characterization of new cellulose nanocrystals from marine biomass Posidonia oceanica. Ind Crops Prod 72:175–182. https://doi.org/10.1016/j.indcrop.2014.12.038

Chaker A, Alila S, Mutjé P et al (2013) Key role of the hemicellulose content and the cell morphology on the nanofibrillation effectiveness of cellulose pulps. Cellulose. https://doi.org/10.1007/s10570-013-0036-y

Chami Khazraji A, Robert S (2013) Interaction effects between cellulose and water in nanocrystalline and amorphous regions: a novel approach using molecular modeling. J Nanomater 2013:409676. https://doi.org/10.1155/2013/409676

Chen P, Wohlert J, Berglund L, Furó I (2022) Water as an intrinsic structural element in cellulose fibril aggregates. J Phys Chem Lett 13:5424–5430. https://doi.org/10.1021/acs.jpclett.2c00781

Cosgrove DJ, Dupree P, Gomez ED, et al (2024) How many glucan chains form plant cellulose microfibrils? A mini review. Biomacromolecules. https://doi.org/10.1021/acs.biomac.4c00995

French AD (2014) Idealized powder diffraction patterns for cellulose polymorphs. Cellulose 21:885–896. https://doi.org/10.1007/s10570-013-0030-4

French AD (2022) How crystalline is my cellulose specimen? Probing the limits of X-ray diffraction. BioResources 17:5557–5561. https://doi.org/10.15376/17.4.5557-5561

Gupta M, Dupree P, Petridis L, Smith JC (2023) Patterns in interactions of variably acetylated xylans with hydrophobic cellulose surfaces. Cellulose 30:11323–11340. https://doi.org/10.1007/s10570-023-05584-z

Hillscher LM, Höfler MV, Gutmann T et al (2024) Influence of TEMPO-oxidation on pulp fiber chemistry, morphology and mechanical paper sheet properties. Cellulose 31:3067–3082. https://doi.org/10.1007/s10570-024-05748-5

Hosoya T, Bacher M, Potthast A et al (2018) Insights into degradation pathways of oxidized anhydroglucose units in cellulose by β-alkoxy-elimination: a combined theoretical and experimental approach. Cellulose 25:3797–3814. https://doi.org/10.1007/s10570-018-1835-y

Hu M, Lv X, Wang Y et al (2024) Recent advance on lignin-containing nanocelluloses: the key role of lignin. Carbohydr Polym 343:122460. https://doi.org/10.1016/j.carbpol.2024.122460

Hubbe MA, Tayeb P, Joyce M et al (2017) Rheology of nanocellulose-rich aqueous suspensions: a review. BioResources 12:9556–9661

Isogai A, Saito T, Fukuzumi H (2011) TEMPO-oxidized cellulose nanofiber. Nanoscale 3:71–85. https://doi.org/10.1039/c0nr00583e

Isogai A, Zhou Y (2019) Diverse nanocelluloses prepared from TEMPO-oxidized wood cellulose fibers: nanonetworks, nanofibers, and nanocrystals. Curr Opin Solid State Mater Sci 23:101–106. https://doi.org/10.1016/j.cossms.2019.01.001

Isogai T, Yanagisawa M, Isogai A (2009) Degrees of polymerization (DP) and DP distribution of cellouronic acids prepared from alkali-treated celluloses and ball-milled native celluloses by TEMPO-mediated oxidation. Cellulose 16:117–127

Kono H, Yunoki S, Shikano T et al (2002) CP/MAS 13C NMR study of cellulose and cellulose derivatives. 1. Complete assignment of the CP/MAS 13C NMR spectrum of the native cellulose. J Am Chem Soc 124:7506–7511. https://doi.org/10.1021/ja010704o

Koskela S, Zha L, Wang S et al (2022) Hemicellulose content affects the properties of cellulose nanofibrils produced from softwood pulp fibres by LPMO. Green Chem 24:7137–7147. https://doi.org/10.1039/D2GC02237K

Kostov KL, Belamie E, Alonso B, Mineva T (2018) Surface chemical states of cellulose, chitin and chitosan studied by density functional theory and high-resolution photoelectron spectroscopy. Bul Chem Commun 50:135–146

Kumagai A, Endo T (2021) Effects of hemicellulose composition and content on the interaction between cellulose nanofibers. Cellulose 28:259–271. https://doi.org/10.1007/s10570-020-03530-x

Lasseuguette E, Roux D, Nishiyama Y (2008) Rheological properties of microfibrillar suspension of TEMPO-oxidized pulp. Cellulose 15:425–433. https://doi.org/10.1007/s10570-007-9184-2

Li K, Clarkson CM, Wang L et al (2021a) Alignment of cellulose nanofibers: harnessing nanoscale properties to macroscale benefits. ACS Nano 15:3646–3673

Li MC, Wu Q, Moon RJ et al (2021b) Rheological aspects of cellulose nanomaterials: governing factors and emerging applications. Adv Mater 33:2006052

Li M-C, Wu Q, Song K et al (2015) Cellulose nanoparticles: structure–morphology–rheology relationships. ACS Sustain Chem Eng 3:821–832. https://doi.org/10.1021/acssuschemeng.5b00144

Lin C, Deng Q, Hu Y et al (2020) Effects of hemicellulose content on TEMPO-mediated selective oxidation, and the properties of films prepared from bleached chemical pulp. Cellulose 27:1043–1054. https://doi.org/10.1007/s10570-019-02844-9

Ludueña LN, Vecchio A, Stefani PM, Alvarez VA (2013) Extraction of cellulose nanowhiskers from natural fibers and agricultural byproducts. Fibers Polym. 14:1118–1127. https://doi.org/10.1007/s12221-013-1118-z

Manian AP, Cordin M, Pham T (2021) Extraction of cellulose fibers from flax and hemp: a review. Cellulose 28:8275–8294. https://doi.org/10.1007/s10570-021-04051-x

Mazega A, Fortuny M, Signori-Iamin G et al (2024) Near-infrared spectroscopy and multivariate analysis as real-time monitoring strategy of TEMPO-mediated oxidation of cellulose fibers from different feedstocks. Cellulose 31:3465–3482

Mazega A, Santos AF, Aguado R et al (2023a) Kinetic study and real-time monitoring strategy for TEMPO-mediated oxidation of bleached eucalyptus fibers. Cellulose 30:1421–1436. https://doi.org/10.1007/s10570-022-05013-7

Mazega A, Signori-Iamin G, Aguado RJ, et al (2023b) Enzymatic pretreatment for cellulose nanofiber production: understanding morphological changes and predicting reducing sugar concentration. Int J Biol Macromol 253. https://doi.org/10.1016/j.ijbiomac.2023.127054

Morais FP, Carta AMMS, Amaral ME, Curto JMR (2021) Micro/nano-fibrillated cellulose (MFC/NFC) fibers as an additive to maximize eucalyptus fibers on tissue paper production. Cellulose 28:6587–6605. https://doi.org/10.1007/s10570-021-03912-9

Naduparambath S, Jinitha TV, Shaniba V, Sreejith MP, Balan AK, Purushothaman E (2018) Isolation and characterisation of cellulose nanocrystals from sago seed shells. Carbohydr Polym 180:13–20. https://doi.org/10.1016/j.carbpol.2017.09.088

Nam S, French AD, Condon BD, Concha M (2016) Segal crystallinity index revisited by the simulation of X-ray diffraction patterns of cotton cellulose Iβ and cellulose II. Carbohydr Polym 135:1–9. https://doi.org/10.1016/j.carbpol.2015.08.035

O'Neill H, Pingali SV, Petridis L et al (2017) Dynamics of water bound to crystalline cellulose. Sci Rep 7:11840. https://doi.org/10.1038/s41598-017-12035-w

Ono Y, Takeuchi M, Zhou Y, Isogai A (2021) TEMPO/NaBr/NaClO and NaBr/NaClO oxidations of cotton linters and ramie cellulose samples. Cellulose 28:6035–6049. https://doi.org/10.1007/s10570-021-03944-1

Pääkkönen T, Dimic-Misic K, Orelma H et al (2016) Effect of xylan in hardwood pulp on the reaction rate of TEMPO-mediated oxidation and the rheology of the final nanofibrillated cellulose gel. Cellulose 23:277–293. https://doi.org/10.1007/s10570-015-0824-7

Park S, Baker JO, Himmel ME et al (2010) Cellulose crystallinity index: measurement techniques and their impact on interpreting cellulase performance. Biotechnol Biofuels 3:10. https://doi.org/10.1186/1754-6834-3-10

Potthast A, Radosta S, Saake B et al (2015) Comparison testing of methods for gel permeation chromatography of cellulose: coming closer to a standard protocol. Cellulose 22:1591–1613. https://doi.org/10.1007/s10570-015-0586-2

Pradhan D, Jaiswal AK, Jaiswal S (2022) Emerging technologies for the production of nanocellulose from lignocellulosic biomass. Carbohydr Polym 285:119258. https://doi.org/10.1016/j.carbpol.2022.119258

Puangsin B, Fujisawa S, Kuramae R et al (2013) TEMPO-mediated oxidation of hemp bast holocellulose to prepare cellulose nanofibrils dispersed in water. J Polym Environ 21:555–563. https://doi.org/10.1007/s10924-012-0548-9

Qiao C, Chen G, Zhang J, Yao J (2016) Structure and rheological properties of cellulose nanocrystals suspension. Food Hydrocoll 55:19–25. https://doi.org/10.1016/j.foodhyd.2015.11.005

Rodionova G, Saito T, Lenes M et al (2013) TEMPO-mediated oxidation of norway spruce and eucalyptus pulps: preparation and characterization of nanofibers and nanofiber dispersions. J Polym Environ 21:207–214. https://doi.org/10.1007/s10924-012-0483-9

Saito T, Isogai A (2004) TEMPO-mediated oxidation of native cellulose: the effect of oxidation conditions on chemical and crystal structures of the water-insoluble fractions. Biomacromol 5:1983–1989. https://doi.org/10.1021/bm0497769

Salmén L (2022) On the organization of hemicelluloses in the wood cell wall. Cellulose 29:1349–1355. https://doi.org/10.1007/s10570-022-04425-9

Sanchez-Salvador JL, Campano C, Balea A et al (2022) Critical comparison of the properties of cellulose nanofibers produced from softwood and hardwood through enzymatic, chemical and mechanical processes. Int J Biol Macromol 205:220–230. https://doi.org/10.1016/j.ijbiomac.2022.02.074

Sang X, Qin C, Tong Z et al (2017) Mechanism and kinetics studies of carboxyl group formation on the surface of cellulose fiber in a TEMPO-mediated system. Cellulose 24:2415–2425. https://doi.org/10.1007/s10570-017-1279-9

Serra A, González I, Oliver-Ortega H, et al (2017) Reducing the amount of catalyst in TEMPO-oxidized cellulose nanofibers: effect on properties and cost. Polymers (Basel) 9. https://doi.org/10.3390/polym9110557

Serra-Parareda F, Tarrés Q, Sanchez-Salvador JL, et al (2021) Tuning morphology and structure of non-woody nanocellulose: Ranging between nanofibers and nanocrystals. Ind Crops Prod 171. https://doi.org/10.1016/j.indcrop.2021.113877

Shibata I, Isogai A (2003) Depolymerization of cellouronic acid during TEMPO-mediated oxidation. Cellulose 10:151–158

Signori-Iamin G, Santos AF, Corazza ML et al (2022) Prediction of cellulose micro/nanofiber aspect ratio and yield of nanofibrillation using machine learning techniques. Cellulose 29:9143–9162

Signori-Iamin G, Santos AF, Mazega A et al (2023) Bayesian-optimized random forest prediction of key properties of micro-/nanofibrillated cellulose from different woody and non-woody feedstocks. Ind Crops Prod 206:117719. https://doi.org/10.1016/j.indcrop.2023.117719

Siller M, Ahn K, Pircher N et al (2014) Dissolution of rayon fibers for size exclusion chromatography: a challenge. Cellulose 21:3291–3301. https://doi.org/10.1007/s10570-014-0356-6

Singh T, Singh AP, Hussain I, Hall P (2013) Chemical characterisation and durability assessment of torrefied radiata pine (Pinus radiata) wood chips. Int Biodeterior Biodegradation 85:347–353. https://doi.org/10.1016/j.ibiod.2013.07.014

Stevens JS, Schroeder SLM (2009) Quantitative analysis of saccharides by X-ray photoelectron spectroscopy. Surf Interface Anal 41:453–462. https://doi.org/10.1002/sia.3047

Sundheq A, Sundherg K, Lillandt C, Holmhom B (1996) Determination of hemicelluloses and pectins in wood and pulp fibres by acid methanolysis and gas chromatography. 11:216–219. https://doi.org/10.3183/npprj-1996-11-04-p216-219

Syverud K, Chinga-Carrasco G, Toledo J, Toledo PG (2011) A comparative study of Eucalyptus and Pinus radiata pulp fibres as raw materials for production of cellulose nanofibrils. Carbohydr Polym 84:1033–1038. https://doi.org/10.1016/j.carbpol.2010.12.066

Tang L, Wang B, Bai S et al (2024) Preparation and characterization of cellulose nanocrystals with high stability from okara by green solvent pretreatment assisted TEMPO oxidation. Carbohydr Polym 324:121485. https://doi.org/10.1016/j.carbpol.2023.121485

Wang Q, Zhong L, Zhou Y et al (2025) Regioselective functionalization of cellulose nanomaterial for advanced application. Carbohydr Polym 348:122889. https://doi.org/10.1016/j.carbpol.2024.122889

Yokota S, Tagawa S, Kondo T (2021) Facile surface modification of amphiphilic cellulose nanofibrils prepared by aqueous counter collision. Carbohydr Polym 255:117342. https://doi.org/10.1016/j.carbpol.2020.117342

Zhou Z, Jaaskelainen AS, Vuorinen T (2008) Oxidation of cellulose and carboxylic acids by hypochlorous acid: kinetics and mechanisms. J Pulp Pap Sci 34:212